Journal of Sound and Vibration 358 (2015) 20–34

Contents lists available at ScienceDirect

Journal of Sound and Vibration

journal homepage: www.elsevier.com/locate/jsvi

Active noise control of a vibrating surface: Continuum and non-continuum investigations on vibroacoustic sound reduction by a secondary heat-flux source

A. Manela *, L. Pogorelyuk

Faculty of Aerospace Engineering, Technion - Israel Institute of Technology, Haifa 32000, Israel

ARTICLE INFO

Article history:
Received 16 March 2015
Received in revised form
6 August 2015
Accepted 15 August 2015
Handling Editor: L. Huang
Available online 4 September 2015

ABSTRACT

We study the effect of surface heating on sound radiation by a vibrating boundary. Focusing on a setup of an infinite planar wall interacting with a semi-infinite expanse of a gas, the system response to arbitrary (small-amplitude) vibro-thermal excitation is investigated. Starting with the case of sinusoidal actuations, the superposed effect of boundary heat-flux excitation at a common frequency ω is examined. The entire range of frequencies is considered, where, depending on the ratio between ω and gas kinetic collision frequency ω_{coll}, fundamentally different flow regimes follow. The two limit cases of $\omega \ll \omega_{\text{coll}}$ (continuum-flow conditions) and $\omega \gg \omega_{\text{coll}}$ (ballistic flow regime) are investigated analytically, based on continuum equations and collisionless Boltzmann equation, respectively. In between, an intermediate interval of frequencies $\omega \sim \omega_{\text{coll}}$ is analyzed numerically, based on the direct simulation Monte Carlo method. In search for optimal conditions for acoustic sound reduction, it is found that effective attenuation is obtained when boundary heat flux is applied at opposite phase to surface actuation. Amplitude-wise, conditions for minimization of the acoustic field vary between the limits: at low-frequency conditions, wave radiation extends over large distances from the wall, and optimal sound reduction is achieved when the ratio between wall-inserted thermal and kinetic energies $|E_q/E_k|_{\text{opt}}$ equals $\gamma/(\gamma-1)$ (with γ denoting the ratio between gas specific heat capacities). At high-frequency conditions, wall signal affects only a thin gas layer (of the order of the mean free path) in the vicinity of the boundary, and optimal attenuation is achieved when $|E_q/E_k|_{\text{opt}} = 1$. The analysis is extended to consider the system response to non-periodic excitations, for the specific case of a delta-function input. Making use of the above collisionless- and continuum-limit analyses, early- and late-time system responses are computed. While conditions for optimal sound reduction at late times coincide with the low-frequency predictions in the periodic case, no counterpart agreement is found between early-time analysis and high-frequency periodic behavior.

© 2015 Elsevier Ltd. All rights reserved.

1. Introduction

Coupling phenomena between structure vibrations, thermal excitations and acoustic radiation are common in numerous scenarios in natural and engineering applications, and have been widely investigated within the disciplines of vibroacoustics [1] and thermoacoustics [2]. Notably, a major part of vibroacoustics literature considers wave propagation in homentropic

* Corresponding author.
E-mail address: amanela@technion.ac.il (A. Manela).

http://dx.doi.org/10.1016/j.jsv.2015.08.016
0022-460X/© 2015 Elsevier Ltd. All rights reserved.

media, by assuming that the thermodynamic description of fluid state does not affect the process of sound radiation. Concurrent studies in thermoacoustics consider acoustic emission from thermal heat sources, with no account taken of body motions as an acoustic source effect. While these separate research disciplines are of fundamental importance, a study on the combined acoustic effects of thermal fluctuations and structural vibrations may be of both theoretical and practical value.

Noise control methodologies for sound reduction of vibrating bodies are traditionally divided into two groups of passive and active systems. In the passive approach, sound reduction is achieved using specifically-designed noise-isolating components, such as noise-damping materials and mufflers [3]. Active control methodologies apply secondary power sources of sound to produce sound waves that interfere with the primary source radiation, and reduce its sound level at desired locations [4,5]. While both approaches are widely common, each has its shortcomings: passive isolating materials, although relatively inexpensive, suffer from low-frequency resonance behavior and are affected in time by mechanical loading of the primary source; active control systems typically supply noise attenuation at only part of the domain, and require the handling and maintenance of additional source powers. These and other limitations have led to ongoing research efforts to develop more efficient noise-control methodologies.

In seeking for new active-noise approaches to control vibroacoustic sound, thermal sound sources have been recently suggested as an effective means to produce sound waves with no moving parts. In a pioneering study, Shinoda [6] has shown that ultrasonic waves may be generated using thermal excitation in solids, where boundary heat flux is prescribed and monitored based on Joule's law of heating. Follow-up works have then investigated the practical feasibility of a "thermoacoustic sound generator", demonstrating its efficiency over a wide range of sound frequencies, and comparing it with counterpart electroacoustic sound generators [7–9]. Building upon this experimentally-validated mechanism, the present work seeks to study the effect of heat-flux sound generation, as a secondary source of sound, to reduce the noise emitted by a reference adiabatic actuated surface. Notably, in recent efforts by Zhao et al. [10,11], the effect of placing a secondary heater on dampening thermoacoustic instabilities in a Rijke tube has been demonstrated. These works have illuminated on the possibility of using thermoacoustic sound, traditionally considered as unwarranted and hazardous byproduct in heat machines [2], as means for beneficial noise monitoring.

In common to almost all works on noise control systems, analyses have been performed based on continuum-flow description of the problems in hand. However, in cases where the time-scale characterizing boundary excitation (or length-scale characterizing the problem of interest) is of the order of the mean free time (or mean free path) of a gas molecule, the continuum description breaks down, and the molecular properties of the gas must be taken into account. Such scenarios are common in micro-scale and low-pressure devices, as well as when considering high-ultrasound radiation. Motivated by these and other applications, analyses of vibroacoustic sound propagation in dilute gas flows have been carried out in the framework of gas kinetic theory (see, e.g., Refs. [12–16], and works cited therein). In a recent contribution by the authors [17], the acoustic effect of combining mechanical actuation with heat-flux boundary excitation has been studied in a confined micro-slab setup, and the efficiency of reducing the total sound radiation has been demonstrated.

To gain further insight into the impact of boundary heat-flux on its total acoustic signature, the present work examines the sound emitted by an actuated and heated surface in a semi-infinite domain. This is fundamentally different from the micro-scale setup studied in Ref. [17], as no characteristic length scale is introduced, apart (possibly) from the wavelength associated with the excitation signal. Both limits of highly-rarefied (for short time-scale excitations) and continuum (for long time-scale perturbations) flow regimes are examined based on varying the input signal, and the relative simple geometric setup enables derivation of closed-form solutions. In particular, different characteristics of sound-wave propagation in rarefied and continuum conditions are illuminated, together with the impact of gas rarefaction on optimal conditions for acoustic sound reduction. The results obtained are validated numerically using the direct simulation Monte Carlo (DSMC) method.

We consider a setup of semi-infinite gas layer interacting with an infinite planar wall, and analyze the gas response to arbitrary small-amplitude vibro-thermal boundary excitation. In Section 2, the collisionless- and continuum-limit problems are formulated, and the numerical DSMC scheme is outlined. Results for periodic (sinusoidal) and non-periodic (impulse) boundary excitations are presented in Sections 3 and 4, respectively. Our conclusions are summarized in Section 5. Some technical details are relegated to an Appendix.

2. Problem formulation

Consider a semi-infinite expanse of perfect monatomic gas confined by an infinite planar surface located at $x^*=0$ (where asterisks denote dimensional quantities). The gas is initially in thermodynamic equilibrium with the surface, with uniform density ρ_0^* and temperature T_0^*. At time $t^*\geq 0$, the boundary is actuated in the normal $\hat{\mathbf{x}}$ direction into the gas layer, according to a prescribed velocity profile,

$$\varepsilon \mathbf{U}_w^*(t^*)=\varepsilon U_w^*(t^*)\hat{\mathbf{x}}. \tag{1}$$

Simultaneously, normal heat-flux is prescribed at the wall

$$\varepsilon \mathbf{Q}_w^*(t^*)=\varepsilon Q_w^*(t^*)\hat{\mathbf{x}}. \tag{2}$$

In (1) and (2), $\varepsilon \ll 1$, so that the system description may be linearized about its initial equilibrium. We seek to analyze the time and space response of the gas to the above vibro-thermal excitation. Depending on the time-scale of exciting signal, the flow regime of signal propagation (rarefied or continuum) is determined. Hereafter we formulate the problem in the two

extreme cases of highly-rarefied (short time-scales) and continuum (long time-scales) conditions. In between, a numerical solution is carried out, based on the DSMC method.

While the present work does not focus on the in-lab application of the above vibro-thermal boundary conditions, some note on the practical realization of the heat-flux condition (2) is in place. In an experiment, direct application of heat-flux at a boundary is normally carried out via the *Joule heating* methodology, mentioned in the Introduction [6–9]. In essence, electric current passing through a metal conductor generates heat with power which equals the product of voltage drop across the element and the current. In this manner, controlling the applied heat flux is equivalent to monitoring the voltage drop across the metal, and can be easily achieved. The temperature variation in this case is unknown, being an outcome of the heat flux and the fluid interaction with the surface. From the theoretical point of view, this approach is relatively less familiar, and many studies apply temperature boundary conditions. We nevertheless prefer heat-flux conditions here since they are more feasible to implement in practice, and enable direct formulation of the problem for adiabatic and non-adiabatic systems, which are of particular interest in the present study.

Before proceeding to the detailed problem formulation, scaling is introduced. In the absence of a macroscopic length scale, the position is scaled by the mean free path of a gas molecule, l^*. In line with present focus on sound-wave propagation, the velocity is scaled by the mean thermal speed of a gas molecule, $U^*_{\rm th}=\sqrt{2R^*T^*_0}$, which is of the order of the speed of sound in the gas. Here R^* marks the specific gas constant. The time is consequently normalized by $l^*/U^*_{\rm th}$, which is of the order of mean free time of a gas molecule [18,19]. Density and temperature are non-dimensionalized by ρ^*_0 and T^*_0, respectively, and the heat flux is normalized by $\rho^*_0 U^{*3}_{\rm th}$.

2.1. Collisionless-flow model

When the time-scale characterizing wall excitation signal is of the order of the mean free time or shorter, the continuum description breaks down, and the molecular description of the gas must be taken into account. Making use of the kinetic theory of gases [18], the gas state is described by the velocity distribution function

$$f(x,t,\mathbf{c})=F[1+\varepsilon\phi(x,t,\mathbf{c})], \tag{3}$$

in which $\mathbf{c}=(c_x,c_y,c_z)$ is the vector of molecular velocity, and $F=\pi^{-3/2}\exp[-c^2]$ is the equilibrium Maxwellian distribution ($c=|\mathbf{c}|$). Assuming the time-scale to be shorter than the mean free time, we neglect the effect of molecular collisions and consider the collisionless Boltzmann equation for $\phi(\mathbf{x},t,\mathbf{c})$,

$$\frac{\partial\phi}{\partial t}+c_x\frac{\partial\phi}{\partial x}=0. \tag{4}$$

The equation is supplemented by an initial condition

$$\phi(x,t=0^-,\mathbf{c})=0, \tag{5}$$

together with an appropriate condition for modeling the interaction between the gas molecules and the surface. Here we make use of the commonly-applied diffuse boundary condition [18], according to which the molecules reflected from the surface (i.e., having $c_x>0$) acquire Maxwellian (equilibrium) distribution characterized by the wall properties (velocity and temperature). In a linearized formulation,

$$\phi(x=0,t,c_x>0)=\rho_w(t)+2c_xU_w(t)+T_w(t)(c^2-3/2), \tag{6}$$

where $U_w(t)$ is obtained from the scaled form of (1), and $\rho_w(t)$ and $T_w(t)$ (the latter being the scaled time-variation of surface temperature perturbation) need to be determined. Since, by definition of the collisionless problem, no interaction occurs between incoming and reflected gas molecules, the velocity distribution perturbation function vanishes for all incoming molecules

$$\phi(x,t,c_x<0)\equiv 0, \tag{7}$$

and only the solution for reflected molecules needs to be followed. Eq. (7) can also be considered as a far-field attenuation condition, ensuring that only causal solution is obtained.

Taking the Laplace transform of (4) and making use of (5) and (6) yield the solution

$$\hat\phi(x,s,c_x>0,c_y,c_z)=\left[\hat\rho_w(s)+2c_x\hat U_w(s)+\hat T_w(s)(c^2-3/2)\right]\exp\left[-sx/c_x\right], \tag{8}$$

where s is the Laplace variable and $\hat{}$ denotes the Laplace transform of a function. By inversion of (8) we obtain

$$\phi(x,t,c_x>0,c_y,c_z)=\rho_w(t_r)+2c_xU_w(t_r)+T_w(t_r)(c^2-3/2), \tag{9}$$

where $t_r=t-x/c_x$ marks the acoustic retarded time. The fields $\rho_w(t)$ and $T_w(t)$ are determined by imposing macroscopic no-penetration and heat-flux conditions

$$\begin{aligned}&\frac{1}{\pi^{3/2}}\int_{-\infty}^{\infty}c_x\phi(x=0)\exp\left[-c^2\right]\mathrm{d}\mathbf{c}=U_w(t)\quad\text{and}\\&\frac{1}{2\pi^{3/2}}\int_{-\infty}^{\infty}c^2c_x\phi(x=0)\exp\left[-c^2\right]\mathrm{d}\mathbf{c}-\frac{5}{4}U_w(t)=Q_w(t),\end{aligned} \tag{10}$$

respectively, at the walls [18]. Substituting Eqs. (7) and (9) into (10) and carrying out all integrations yield closed-form expressions for $\rho_w(t)$ and $T_w(t)$,

$$\rho_w(t)=\sqrt{\pi}\left(\frac{7}{8}U_w(t)-Q_w(t)\right) \quad \text{and} \quad T_w(t)=\sqrt{\pi}\left(\frac{1}{4}U_w(t)+2Q_w(t)\right). \tag{11}$$

With $\rho_w(t)$ and $T_w(t)$ obtained, the probability density function ϕ in (9) is known, and the $O(\varepsilon)$ perturbations of all hydrodynamic fields can be computed through appropriate quadratures over the molecular velocity space [18]. Defining

$$I_n=\int_0^\infty U_w(t_r)c_x^n\exp[-c_x^2]\,\mathrm{d}c_x, \quad J_n=\int_0^\infty \rho_w(t_r)c_x^n\exp[-c_x^2]\,\mathrm{d}c_x$$
$$\text{and} \quad K_n=\int_0^\infty T_w(t_r)c_x^n\exp[-c_x^2]\,\mathrm{d}c_x, \tag{12}$$

the expressions for the density, velocity and pressure perturbations are given by

$$\rho(x,t)=\frac{1}{\sqrt{\pi}}\left(2I_1+J_0+K_2-\frac{1}{2}K_0\right), \tag{13}$$

$$u(x,t)=\frac{1}{\sqrt{\pi}}\left(2I_2+J_1+K_3-\frac{1}{2}K_1\right) \tag{14}$$

and

$$p(x,t)=\frac{2}{3\sqrt{\pi}}\left(2(I_3+I_1)+J_2+J_0+K_4+\frac{1}{2}(K_2+K_0)\right), \tag{15}$$

respectively. The temperature perturbation is obtained using the linearized form of the gas equation of state,

$$T=p-\rho. \tag{16}$$

2.2. Continuum model

Assuming that the characteristic time-scale for wall input signal is much larger than the mean free time, continuum conditions prevail, and the Navier–Stokes–Fourier equations are applied. Making use of the scaling introduced in the beginning of Section 2, and linearizing about the initial equilibrium state, we obtain the following unsteady one-dimensional balances of mass, momentum and energy for the $O(\varepsilon)$ density, normal velocity and temperature perturbations,

$$\frac{\partial\rho}{\partial t}+\frac{\partial u}{\partial x}=0, \tag{17}$$

$$\frac{\partial u}{\partial t}=-\frac{1}{2}\left(\frac{\partial\rho}{\partial x}+\frac{\partial T}{\partial x}\right)+\frac{4}{3\alpha}\frac{\partial^2 u}{\partial x^2}, \tag{18}$$

and

$$\frac{\partial T}{\partial t}=\frac{\gamma}{\alpha Pr}\frac{\partial^2 T}{\partial x^2}-(\gamma-1)\frac{\partial u}{\partial x}. \tag{19}$$

The pressure perturbation is given by the linearized form of the equation of state, $p=\rho+T$. In (18) and (19),

$$\alpha=\frac{\rho_0^* U_{\mathrm{th}}^* l^*}{\mu_0^*}, \quad Pr=\frac{\mu_0^* c_p^*}{k_0^*} \quad \text{and} \quad \gamma=\frac{c_p^*}{c_v^*}, \tag{20}$$

where μ_0^* denotes the mean dynamic viscosity of the gas, and c_p^* and c_v^* mark its specific heat capacities at constant pressure and volume, respectively. For the perfect monatomic gas considered here, the Prandtl number $Pr=2/3$ and $\gamma=5/3$. The non-dimensional parameter α (which replaces the Reynolds number in the absence of a macroscopic length-scale) depends on the gas model of molecular interaction. Focusing on a case of a hard-sphere gas, $\alpha=16/(5\sqrt{\pi})$ [19]. Having fixed the non-dimensional parameters in (20), the problem is governed by the acoustic input signal, which fixes the boundary conditions of wall impermeability and heat-flux

$$u=U_w(t) \quad \text{and} \quad \frac{\partial T}{\partial x}=2\alpha Pr\frac{\gamma-1}{\gamma}Q_w(t) \quad \text{at } x=0, \tag{21}$$

respectively. By applying conditions (21), we assume the boundary to be “ideal” (as also assumed in Section 2.1 for a collisionless gas), in the sense that its mechanical and thermal properties are not coupled to the gas layer dynamics. Such effects (which have been modeled in part of the thermoacoustic analyses cited in Section 1, e.g. [8]) may be taken into account in a more detailed modeling of the solid–gas interaction, yet are not in the scope of the present contribution. Problem formulation is completed by imposing far-field ($x\to\infty$) attenuation conditions for all perturbations.

The problem is analyzed by applying the time Fourier transform

$$\overline{G}(\omega)=\int_{-\infty}^{\infty}G(t)\exp[-\mathrm{i}\omega t]\,\mathrm{d}t, \tag{22}$$

to Eqs. (17)–(21). This yields a system of ordinary equations

$$\mathrm{i}\omega\overline{\rho}+\overline{u}'=0,\quad \mathrm{i}\omega\overline{u}=-\frac{1}{2}\left(\overline{\rho}'+\overline{T}'\right)+\frac{4}{3\alpha}\overline{u}'',\quad \mathrm{i}\omega\overline{T}=\frac{\gamma}{\alpha Pr}\overline{T}''-(\gamma-1)\overline{u}', \tag{23}$$

where primes denote differentiations with respect to x, accompanied by wall-excitation boundary conditions

$$\overline{u}(x=0)=\overline{U}_w(\omega)\quad\text{and}\quad \overline{T}'(x=0)=2\alpha Pr\frac{\gamma-1}{\gamma}\overline{Q}_w(\omega), \tag{24}$$

and far-field attenuation conditions. Here primes denote differentiations with respect to x. The density and velocity perturbations can be eliminated using

$$\overline{\rho}=\frac{\mathrm{i}}{\omega}\overline{u}'\quad\text{and}\quad \overline{u}=-\frac{\mathrm{i}\gamma}{\omega(\gamma-1)\alpha Pr}\left(\frac{4}{3\alpha}-\frac{\mathrm{i}}{2\omega}\right)\overline{T}'''+\frac{\mathrm{i}}{\omega(\gamma-1)}\left(\frac{\gamma}{2}+\frac{4\mathrm{i}\omega}{3\alpha}\right)\overline{T}', \tag{25}$$

to yield a single equation for the temperature:

$$a_2\overline{T}'''+a_1\overline{T}''+a_0\overline{T}=0. \tag{26}$$

In (26),

$$a_2=\frac{\mathrm{i}\gamma}{\omega\alpha Pr}\left(\frac{4}{3\alpha}-\frac{\mathrm{i}}{2\omega}\right),\quad a_1=-\frac{\mathrm{i}}{\omega}\left(\frac{\gamma}{2}+\frac{4\mathrm{i}\omega}{3\alpha}\right)+\frac{\gamma}{\alpha Pr},\quad a_0=-\mathrm{i}\omega\,. \tag{27}$$

The biquadratic characteristic equation of (26) has four distinct roots, out of which only two have negative real parts that satisfy the far-field attenuation condition. Denoting

$$r_1(\omega)=\left[\frac{-a_1+\sqrt{a_1^2-4a_2a_0}}{2a_2}\right]^{1/2}\quad\text{and}\quad r_2(\omega)=\left[\frac{-a_1-\sqrt{a_1^2-4a_2a_0}}{2a_2}\right]^{1/2}, \tag{28}$$

the general attenuating solution for the transformed temperature perturbation is given by

$$\overline{T}(x,\omega)=D_1(\omega)\exp[r_1(\omega)x]+D_2(\omega)\exp[r_2(\omega)x]. \tag{29}$$

The coefficients D_1 and D_2 are obtained by imposing wall impermeability and heat-flux conditions (24), yielding

$$D_1(\omega)=\frac{\overline{U}_w-c_3\overline{Q}_w(c_1r_2^2+c_2)}{c_1r_1(r_1^2-r_2^2)}\quad\text{and}\quad D_2(\omega)=\frac{c_3\overline{Q}_w-D_1r_1}{r_2}, \tag{30}$$

where

$$c_1=-\frac{\mathrm{i}\gamma}{\omega(\gamma-1)\alpha Pr}\left(\frac{4}{3\alpha}-\frac{\mathrm{i}}{2\omega}\right),\quad c_2=\frac{\mathrm{i}}{\omega(\gamma-1)}\left(\frac{\gamma}{2}+\frac{4\mathrm{i}\omega}{3\alpha}\right),\quad c_3=2\alpha Pr\frac{\gamma-1}{\gamma}\,. \tag{31}$$

Expressions for the Fourier-transformed density and velocity perturbations now follow by substitution of Eq. (29) into (25). The transformed pressure perturbation is given by $\overline{p}=\overline{\rho}+\overline{T}$. The time-domain solution is obtained by taking the real part of the inverse Fourier transform

$$G(t)=\frac{1}{2\pi}\int_{-\infty}^{\infty}\overline{G}(\omega)\exp[\mathrm{i}\omega t]\,\mathrm{d}\omega, \tag{32}$$

of each of the transformed hydrodynamic fields.

2.3. Monte-Carlo simulations

The DSMC method is a stochastic particle method commonly used for studying rarefied and continuum-limit gas flows [20]. The method is applied here to verify the accuracy of limit-case results obtained in Sections 2.1 and 2.2, and examine their validity with departure from limit conditions. Based on the mean-free-path scaling introduced in the beginning of Section 2, it is expected that the collisionless-limit results will be valid when the characteristic time-scale of acoustic input signal is small compared with the mean free time ($t_{\mathrm{char}}\ll1$), and in the vicinity of the boundary, $x\ll1$; at the other extreme, the continuum-based model is expected to be effective only at far-enough distances from the wall, $x\gg1$, as well as when excitation time-scales are large compared with the mean free time, $t_{\mathrm{char}}\gg1$. The DSMC scheme, with which the analytical results are compared, is considered numerically “exact”, and therefore allows for accurate numerical analysis also at intermediate conditions of $O(1)$ values of time and place.

During simulations, a one-dimensional version of the DSMC scheme was employed to calculate the response of a hard-sphere gas to prescribed boundary excitation. Fully diffuse boundary conditions were imposed at the surface [18,20]. To make use of the standard DSMC algorithm in a confined domain, only a finite region near the boundary was simulated. The location of an outer "virtual" boundary was chosen far enough from the perturbed surface so that its influence on the results could not be detected. Isothermal (equilibrium) boundary conditions were imposed at the far-field boundary, and it has been verified that the results were not affected by displacing it further away from the perturbed surface. For the case of periodic excitation simulated in the present work (see Section 3), DSMC results were obtained by taking an ensemble average over a large number of time periods. The algorithm applied for controlling the heat flux at a boundary (required for implementing the heat-flux boundary condition) was identical to the one described in Ref. [17]. A typical simulation lasted several hours using a 24 Intel Xeon E5645 cores machine, and consisted of approximately 10^9 simulated particles.

3. Periodic excitation

Consider the case of sinusoidal excitation, where mechanical and thermal wall inputs are applied with common frequency ω and phase difference φ

$$U_w(t)=U_0\ \cos(\omega t)\quad\text{and}\quad Q_w(t)=Q_0\ \cos(\omega t+\varphi), \tag{33}$$

and U_0 and Q_0 determine their ε-scaled amplitudes, respectively (see Eqs. (1)–(2)). The problem dependence on the input frequency ω specifies the characteristic time-scale of system response, $t_{\text{char}}\approx\omega^{-1}$. In line with the discussion in Section 2.3, the collisionless solution is expected to be valid for $\omega\gg1$, while continuum conditions should prevail for $\omega\ll1$. We follow on these limits and seek to find the optimal conditions in which the pressure disturbance is minimized in each. The intermediate domain of $\omega\sim O(1)$ is then also considered.

Our calculations uniformly indicate that, for the purpose of achieving optimal reduction of the emitted sound, heat-flux excitation should be employed in counter phase (i.e., with $\varphi=\pi$) to boundary vibrations. This result is physically reasonable, and shows that, to cancel out a pressure wave generated by a boundary displaced into the gas domain, heat should be removed from the medium, and *vice versa*. For brevity, we therefore consider here only cases where Q_0 has a sign equal (equivalent to $\varphi=0$) or opposite (equivalent to $\varphi=\pi$) to U_0. In an actual experiment, given that the generation of each of the two signals is controlled independently, it should be feasible to combine them with prescribed phase shift. One possible difficulty in doing so may be an inevitable phase-lag occurring between the two signals, resulting from the geometrical setup of the system. This may be overcome by initial system calibration, where the phase of one signal is fixed and the phase of the other is continuously varied, to achieve optimal conditions.

3.1. High-frequency limit

Substituting Eq. (33) into Eqs. (13)–(16) and carrying out the integrals defined in Eq. (12), the collisionless solution is obtained. Strictly, since boundary excitation is initiated at $t=0$, the system exhibits initial transient behavior before reaching its final periodic state. Yet, we here consider only the "late-time" periodic behavior. Our calculations, supported by DSMC predictions, indicate that the system reaches its periodic state after only few periods.

In addition to numerical calculation of the integrals in Eqs. (13)–(15), the time-periodic solution can also be evaluated asymptotically for high frequencies. Making use of the steepest descent analysis presented by Abramowitz [21], we find, for $\omega x\gg1$,

$$\begin{aligned}G_n&=\int_0^\infty\cos(\omega t_r)c_x^n\exp\left[-c_x^2\right]\mathrm{d}c_x=\mathrm{Re}\left\{\exp[\mathrm{i}\omega t]\int_0^\infty c_x^n\exp[-\mathrm{i}\omega x/c_x-c_x^2]\,\mathrm{d}c_x\right\}\\&\approx\mathrm{Re}\left\{\sqrt{\frac{\pi}{3}}3^{-n/2}z^{n/2}\left(1+\frac{a_1}{z}+\frac{a_2}{z^2}+O\left(z^{-3}\right)\right)\exp[\mathrm{i}\omega t-z]\right\},\end{aligned} \tag{34}$$

where

$$z=3(\omega x/2)^{2/3}\exp[\mathrm{i}\pi/3],\quad a_1=(3n^2+3n-1)/12,$$
$$\text{and}\quad a_2=(9n^4+6n^3-51n^2-24n+25)/288,$$

and $\mathrm{Re}\{\cdot\}$ marks the real part of a complex number. Substituting (34) together with (11) and (33) into (12) and then into (13)–(16), we obtain the high-frequency approximation for the hydrodynamic perturbations detailed in the Appendix. Notably, all fields decay exponentially with distance from the wall with rate $\sim(\omega x)^{1/3}\exp[-(\omega x)^{2/3}]$, as inferred from Eq. (34). For $\omega\gg1$, this decay confines the "penetration depth" of the acoustic signal to a narrow layer in the vicinity of the wall. In accordance with collisionless-flow approximation, this layer becomes of the order of the mean free path or less in the present limit (see Fig. 1).

While approximation (34) is valid away from the wall (where $\omega x\gg1$ for large ω), evaluation of the system response in the proximity of the boundary is also of interest. Regardless of the value of ω, expansion (34) becomes invalid at the wall, where

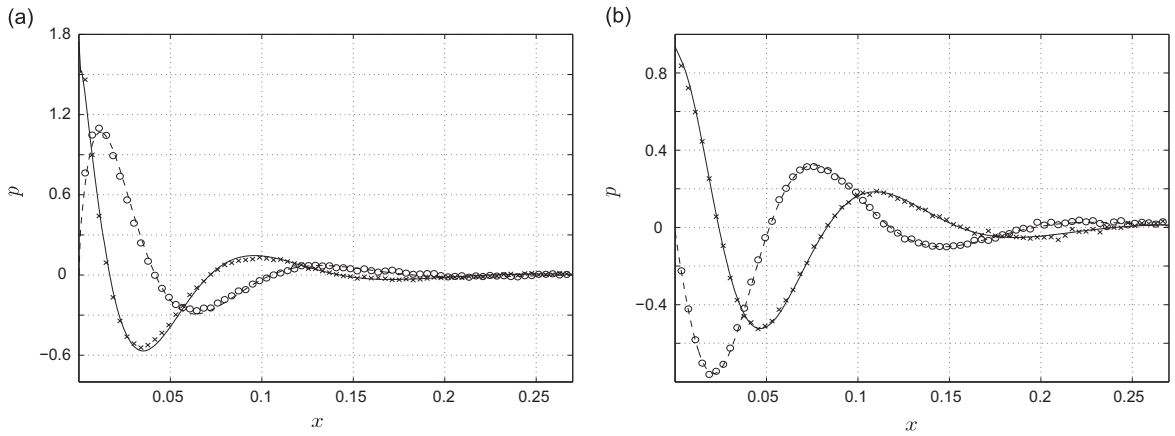

Fig. 1. Comparison between collisionless (solid and dashed lines) and DSMC (crosses and circles) predictions for the pressure perturbation in response to $\omega=91.3$ sinusoidal excitation (see (33)): (a) adiabatic animation ($U_0=1, Q_0=0$); (b) heat-flux excitation ($U_0=0, Q_0=1$). Solid (crosses for DSMC) and dashed (circles for DSMC) curves mark pressure distributions at times $t=2\pi n/\omega$ and $t=(2\pi n+\pi/2)/\omega$, respectively ($n=1,2,\ldots$).

$\omega x=0$. Using Eqs. (13), (15) and (16), exact calculation of the density, temperature and pressure perturbations at $x=0$ yields

$$\rho(0,t)=\frac{1}{\sqrt{\pi}}\left[\left(1+\frac{7\pi}{16}\right)U_0-\frac{\pi}{2}Q_0\right]\cos(\omega t),\quad T(0,t)=\frac{1}{\sqrt{\pi}}\left[\left(\frac{1}{3}+\frac{\pi}{8}\right)U_0+\pi Q_0\right]\cos(\omega t)$$
$$\text{and}\quad p(0,t)=\frac{2}{3\sqrt{\pi}}\left[\left(2+\frac{27\pi}{32}\right)U_0+\frac{3\pi}{4}Q_0\right]\cos(\omega t). \tag{35}$$

For later reference we note that minimization of the density, temperature and pressure perturbations at the wall occur at different values of the ratio between heat flux and velocity input amplitudes, $|Q_0/U_0|$. Specifically, the pressure perturbation at the wall vanishes for $|Q_0/U_0|\approx 1.97$.

To test the validity of the collisionless approximation, Fig. 1 compares between predictions of the above solution and DSMC calculations for the pressure perturbation at high-frequency conditions, $\omega=91.3$. In Fig. 1a, results are shown for adiabatic boundary actuation with $U_0=1$ and $Q_0=0$, and in Fig. 1b, the case of heat-flux excitation with $U_0=0$ and $Q_0=1$ is considered. Both figures compare the x-distribution of acoustic pressure at the beginning of a period ($t=2\pi n/\omega, n=1,2,\ldots$) and at quarter time of a period ($t=(2\pi n+\pi/2)/\omega, n=1,2,\ldots$). The analytical results presented are based on direct numerical evaluation of the integral expression (15) for $p(x,t)$. We have verified that these results match with the "far-field" asymptotic evaluation presented in the Appendix for $x>0.01$ (corresponding to $\omega x>1$), as well as with the exact $x=0$ expression in Eq. (35). The agreement between analytical and DSMC findings is generally very good. Small discrepancies are observed for $x\gtrsim 0.2$ (particularly in Fig. 1b), resulting from the inherent statistical noise in DSMC calculations, visible at the small values of the pressure obtained at these locations.

Comparing between waveforms Fig 1a and b, we observe a similar fast-decaying signal behavior in response to both adiabatic and heat-flux excitations. In line with approximation (34), the pressure decays to a vanishingly small value already at $x\approx 0.25$, only one-fourth of a free path away from the wall. Similar decay rate characterizes all other hydrodynamic perturbations as well. Given that the acoustic wave propagates in the mean thermal speed at collisionless conditions [17], the scaled acoustic wavelength for the present frequency is given by $\lambda=2\pi/\omega\approx 0.069$. It is therefore observed that the signal penetrates only three to four wavelengths into the gas layer. Our calculations indicate that a similar qualitative result is also obtained in response to other high-frequency excitations.

For the purpose of minimizing the acoustic pressure induced by boundary oscillations, we superpose the signal obtained in Fig. 1a with the thermoacoustic signal shown in Fig. 1b multiplied by the control parameter Q_0. Focusing on the "far-field" signal, Fig. 2 presents perturbations amplitude variations, at fixed locations, with Q_0, for two different high frequency values ($\omega=91.3$ in Fig. 2a and $\omega=18.3$ in Fig. 2b), and two different locations ($x=0.16$ and $x=1$), respectively. In terms of acoustic wavelength, both x-locations are chosen between two and three wavelengths away from the boundary, which is considered "far field" for the high-frequency analysis. At these relatively far locations, comparison with DSMC findings proves inefficient, owing to relatively high noise levels in the numerical solution, and is therefore not presented here.

The main finding of Fig. 2 is in a distinct minimum observed in perturbation amplitudes, common to all hydrodynamic fields, at $Q_0=-0.5$. Thus, the choice $Q_0=-0.5$ appears optimal for far-field pressure reduction, regardless of the value of $\omega\gg 1$. To rationalize this result, we introduce expressions for dimensional wall-inserted kinetic and thermal energies (per unit area) transferred to the gas during a time interval $t^*\in[0,t_f^*]$. These are given by

$$E_k^*=\int_0^{t_f^*} p_0^* U_w^*(t^*)\,\mathrm{d}t^*\quad\text{and}\quad E_q^*=\int_0^{t_f^*} Q_w^*(t^*)\,\mathrm{d}t^*, \tag{36}$$

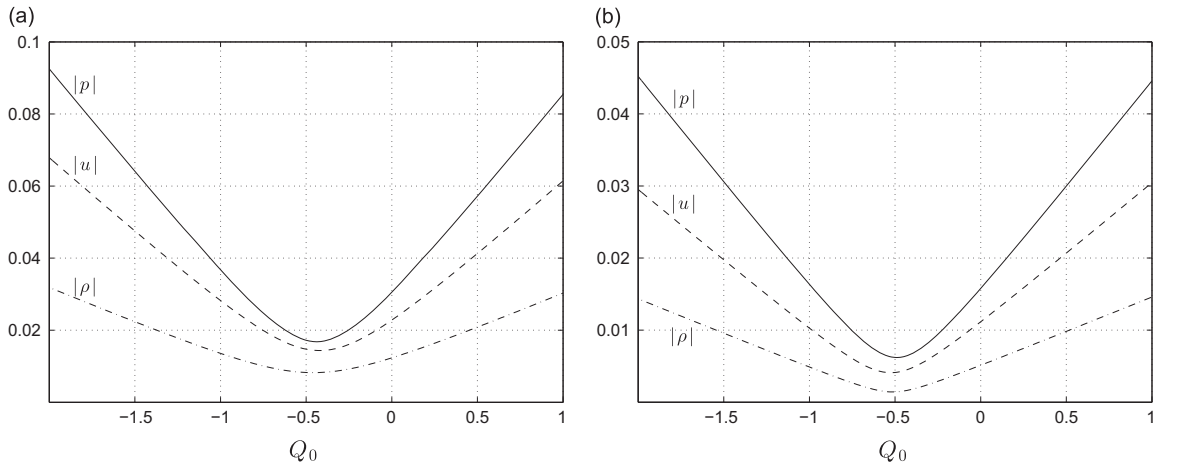

Fig. 2. Variations at fixed locations of the pressure (solid lines), velocity (dashed lines) and density (dash-dotted lines) perturbation amplitudes with amplitude of sinusoidal heat-flux excitation Q_0. In both cases, the surface is actuated with amplitude $U_0=1$ (see Eq. (33)). In (a), $\omega=91.3$ and $x=0.16$; in (b), $\omega=18.3$ and $x=1$.

respectively, where $p_0^*=\rho_0^* R^* T_0^*$ marks the equilibrium gas pressure. Substituting Eq. (33) in its dimensional form into Eq. (36) and dividing, we obtain

$$\left|\frac{E_q^*}{E_k^*}\right|=\left|\frac{2Q_0}{U_0}\right|. \tag{37}$$

Notably, at the above-found optimal value of Q_0 (with $U_0=1$)

$$\left|Q_0^{\mathrm{opt}}(\omega\gg 1)\right|=U_0/2, \tag{38}$$

the ratio (37) becomes

$$\left|\frac{E_q^*}{E_k^*}\right|^{\mathrm{opt}}_{\omega\gg 1}=1. \tag{39}$$

It is therefore concluded that, at high-frequency conditions, optimal reduction in motion-induced sound is obtained when thermal energy is inserted with amplitude equal to kinetic energy. The negative sign of optimal indicates that, as mentioned above, heat should be inserted in opposite phase compared with actuation signal: specifically, heat should be removed when the boundary moves into the gas, and invested when the boundary is actuated outwards.

While the above result may seem expected, it will be shown in the next section that different optimal conditions for sound reduction are required at low frequencies. In between the two limits, an intermediate range of frequencies exists, where the system response combines properties from the two regimes (see Section 3.3).

3.2. Low-frequency limit

The frequency-domain solution obtained in Section 2.2 for a single Fourier component can be applied to obtain the time-domain response to sinusoidal excitation at times when the system has reached its periodic state. In this section we focus on the limit of low frequencies, $\omega\lesssim 0.1$, to test the validity of the analytical solution compared with DSMC predictions. Recalling that the time-scale used for problem non-dimensionalization, l^*/U_{th}^*, is of the order of the mean free time (see the beginning of Section 2), it is noted that the upper limit of frequencies considered in this section is only one order of magnitude lower than the mean collision frequency. At standard conditions, these frequencies correspond to dimensional quantities that are at the high ultrasound regime.

In parallel with Fig. 1, Fig. 3 presents a comparison between continuum and DSMC predictions for gas acoustic pressure in response to $\omega=0.09$ sinusoidal excitation with different choices of the boundary conditions: Fig. 3a considers adiabatic boundary actuation (where $U_0=1$ and $Q_0=0$), and Fig. 3b shows results for heat-flux excitation of a stationary boundary ($U_0=0$ and $Q_0=1$). In addition, Fig. 3c presents our predictions for combined vibro-thermal excitation with $U_0=1$ and $Q_0=\gamma/(2(\gamma-1))$. In each case, the spatial distribution of the acoustic pressure is presented at the beginning ($t=2\pi n/\omega, n=1,2,\ldots$) and at quarter time ($t=(\pi/2+2\pi n)/\omega$) of a period.

Starting with Figs. 3a and b, we observe similar oscillatory-decaying behavior of the acoustic wave in response to both mechanical and thermal excitations. The decay in perturbation amplitudes with distance from the of wall is relatively slow in terms of the chosen mean-free-path scale, extending beyond the $x\in[0,300]$ interval presented. This decay rate is orders of magnitude slower than in the high-frequency case presented in Fig. 1. The overall agreement between continuum-based

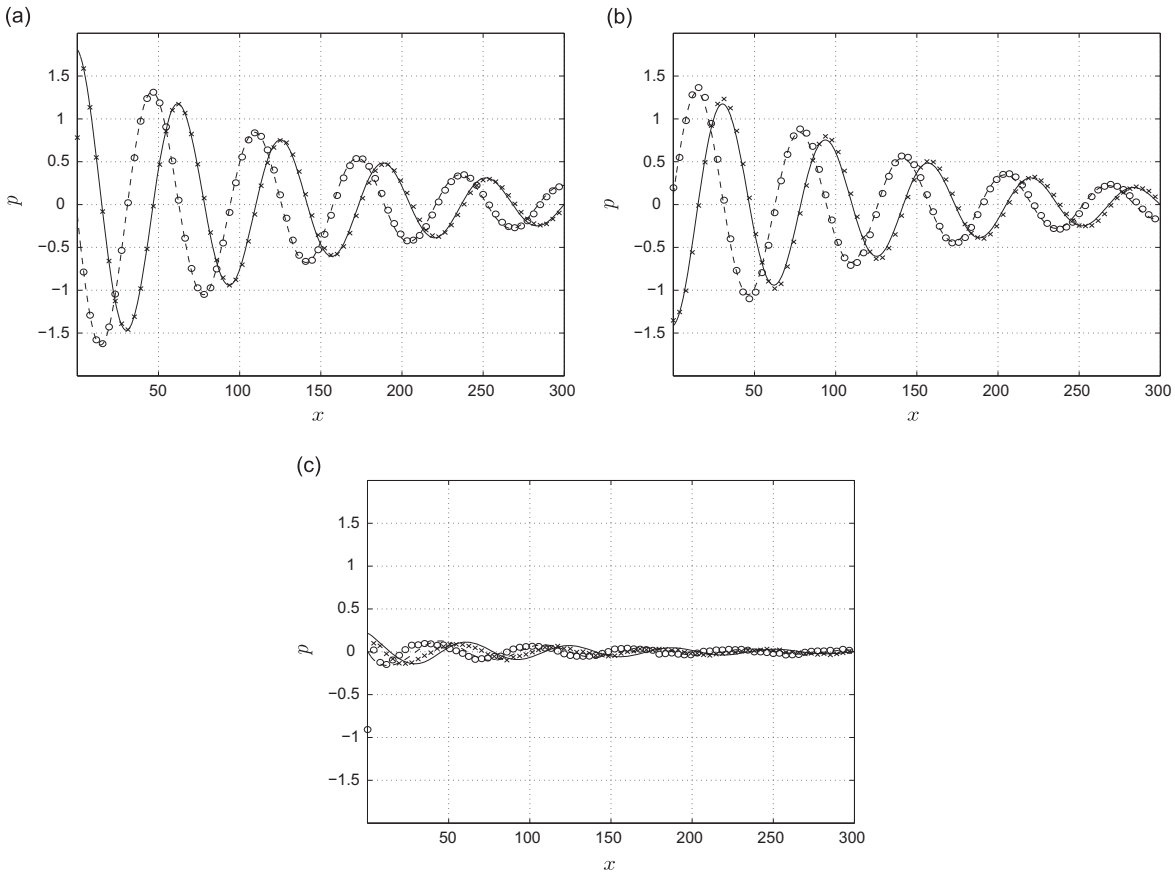

Fig. 3. Comparison between continuum (solid and dashed lines) and DSMC (crosses and circles) predictions for the pressure perturbation in response to $\omega=0.09$ sinusoidal excitation (see (33)): (a) adiabatic actuation ($U_0=1, Q_0=0$); (b) heat-flux excitation ($U_0=0, Q_0=1$); (c) optimal sound-reduction conditions ($U_0=1, Q_0=\gamma/(2(\gamma-1))$). Solid (crosses for DSMC) and dashed (circles for DSMC) curves mark pressure perturbations at times $t=2\pi n/\omega$ and $t=(2\pi n+\pi/2)/\omega$, respectively ($n=1,2,\ldots$).

and DSMC predictions is very good, in support of the analytical solution. Small discrepancies are nevertheless viewed close to the near-wall maximum points, which result from the relatively large frequency value considered (in view of the continuum conditions assumed for the analysis), and associated short characteristic time and local length scales.

Similar to the discussion in Section 3.1, we seek for optimal conditions on the heat-flux amplitude Q_0 to minimize the vibroacoustic pressure disturbance in Fig. 3a. Towards this end, we consider the limit $\omega\to 0$, where the continuum-model predictions are *a fortiori* valid. Strictly, the low-frequency limit corresponds to a quasistatic process, where wall excitation period extends over an infinitely long time. For an adiabatic boundary, the system is thermally insulated; the additional (reversible) effect of surface heat-flux is hereby considered.

The results in Figs. 1 and 2 indicate that, with decreasing ω, the spatial decay rate of wall-induced oscillations decreases, so that wall excitation affects a wider gas layer. Applying the $\omega\ll 1$ limit to expressions (25)–(31) and taking $x\gg 1$, we find that expression (29) for the Fourier-transformed temperature perturbation is dominated by the r_1-exponent part. Reverting to the time domain, we obtain

$$T(x,t)\approx D_1\exp\left[\mathrm{i}\omega\left(t-\sqrt{2/\gamma}x\right)-\omega^2\kappa x\right], \tag{40}$$

together with

$$u(x,t)\approx\frac{\sqrt{2/\gamma}}{\gamma-1}T(x,t)\quad\text{and}\quad\rho(x,t)\approx\sqrt{2/\gamma}u(x,t). \tag{41}$$

The decay constant κ appearing in (40) is given by

$$\kappa=\frac{1}{2\alpha}\left(\frac{2}{\gamma}\right)^{3/2}\left(\frac{2}{3}+\frac{1}{Pr}-\gamma\right), \tag{42}$$

which equals ≈ 0.182 for the present hard-sphere gas model (see (20) *et seq.*). The form of far-field solution (40)–(42) therefore represents a slowly-decaying propagating wave. The wave propagates with the speed of sound, $c_0^*=\sqrt{\gamma R^* T_0^*}$, and

the factor $\sqrt{2/\gamma}$ arises owing to the scaling of the velocity by the mean thermal speed, $U^*_{\rm th}=\sqrt{2R^*T^*_0}$ (see Section 2). In terms of the quasistatic limit considered, the $\exp[-\omega^2 kx]$ decay factor is regarded as a "high-order" effect. This decay rate is functionally different from the $\sim(\omega x)^{1/3}\exp\left[-(\omega x)^{2/3}\right]$ decay found in the high-frequency limit discussed in Section 3.1 (see Eq. (34) *et seq.*).

To minimize the actuation-induced far-field pressure, we observe that the vanishing of $p=\rho+T$ in the quasistatic approximation is achieved when $D_1(\omega)=0$. Making use of Eq. (30), and taking the limit $\omega\ll 1$, an optimized value for the heat-flux amplitude is obtained by canceling the leading-order pressure,

$$\left|Q_0^{\rm opt}(\omega\ll 1)\right|=\left|\frac{1}{c_3(c_1r_2^2+c_2)}U_0\right|\approx\left|\frac{\gamma}{2(\gamma-1)}U_0\right|. \tag{43}$$

The result in (43) is confirmed by the findings in Fig. 3c, which show a uniformly low pressure perturbation for $U_0=1$ and $Q_0=\gamma/(2(\gamma-1))$ at $\omega\approx 0.09$. As in the high-frequency limit, the optimal value of Q_0 is independent of the frequency of oscillations, as long as ω, in this case, is low enough, so that continuum conditions prevail. Supported by the agreement between analytical and DSMC results in Fig. 3, these conditions hold for frequencies as high as $\omega\approx 0.1$, above which the continuum description breaks down and an intermediate regime of response takes place (see Section 3.3). Any frequency-dependence of the optimal value of Q_0 for sound monitoring at $\omega\ll 1$ is relegated to a higher $O(\omega)$ correction of Eq. (43), negligible in the present limit.

To rationalize the above finding, we consider the limit $\omega\to 0$ from a thermodynamic point of view. Placing a "virtual" adiabatic piston in the far field, we apply the first law of thermodynamics to the system. Assuming quasistatic conditions, the dimensional energy balance reads

$$c_p^*\,{\rm d}T^*=p_0^*\,{\rm d}v^*+c_v^*\,{\rm d}T^*, \tag{44}$$

equating the amount of heat invested in the system with the sum of work done by the moving surfaces and the total change in system internal energy. In the case of an oscillating adiabatic surface, balance (44) becomes trivial: no heat enters the system, and the net amount of work done by the gas is zero, with both animated and "virtual" boundaries moving in parallel motion. However, the balance changes when considering the thermoacoustic problem of a heated stationary surface: using Eq. (44) and the relation $R^*=c_p^*-c_v^*$ for an ideal gas, the ratio between the work done by the moving far-field piston and the amount of heat transferred to the system by the excited wall is

$$\frac{R^*\,{\rm d}T^*}{c_p^*\,{\rm d}T^*}=\frac{\gamma-1}{\gamma}. \tag{45}$$

This can be referred to as the relative part of inserted thermal energy which is transmitted into sound in the far field. Recalling the general expression (37) for the ratio between wall-inserted thermal and kinetic energies, we find that, at the optimal conditions specified by Eq. (43),

$$\left|\frac{E_q^*}{E_k^*}\right|^{\rm opt}_{\omega\ll 1}=\frac{\gamma}{\gamma-1}, \tag{46}$$

which is the inverse of the ratio in Eq. (45). It is therefore for the optimal choice (43) of $Q_0=Q_0^{\rm opt}(\omega\ll 1)$ that the far-field energy of a heat-excited wave equals the energy of a counterpart motion-excited wave. At these equal energy levels, the two acoustic waves may cancel each other in the far field when generated at an opposite phase. Clearly, the optimal conditions for sound reduction at $\omega\ll 1$ are qualitatively different, and reflect on a different mechanism of sound wave propagation, from those obtained for $\omega\gg 1$ (cf. Eqs. (43), (46) and (38), (39), respectively). The difference stems from a partial transfer of wall thermal energy into gas internal energy (denoted by the $c_v^*\,{\rm d}T^*$ term in (44)), absent at high frequencies. In the latter case, wall thermal energy is transferred entirely into sound, as discussed in Section 3.1.

The above analysis should be considered as a leading-order approximation at quasistatic conditions, $\omega\to 0$. In practice, there exists an $O(\omega)$ correction to the calculation, which is not followed here. With increasing ω, the effect of this correction becomes significant; yet, simultaneously, the continuum description breaks down. The next section discusses the system response at such intermediate values of $\omega\sim O(1)$, where neither the continuum (Section 3.2) nor the collisionless (Section 3.1) limit analyses hold.

3.3. Intermediate regime

Having demonstrated the validity of collisionless (high frequency) and continuum (low frequency) analyses in Sections 3.1 and 3.2, we now discuss the system response to $\omega\sim O(1)$ excitation. To this end, Fig. 4 presents the spatial distribution of acoustic pressure in response to periodic boundary excitation with $\omega=1$. Fig. 4a focuses on the case of adiabatic boundary actuation, and presents comparison between DSMC, continuum-limit and collisionless-limit predictions. Fig. 4b compares between DSMC results for the pressure signal in response to adiabatic (as in Fig. 4a) and vibro-thermal excitations. In the latter,

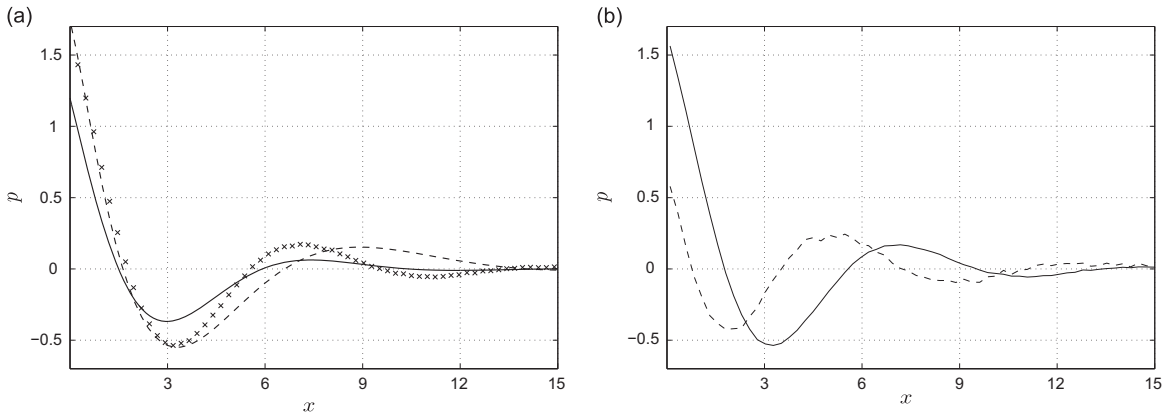

Fig. 4. (a) Comparison between DSMC (crosses), continuum-limit (solid line) and collisionless-limit (dashed line) predictions for the pressure perturbation in response to sinusoidal adiabatic actuation with $U_0=1$ and $Q_0=0$ at $\omega=1$. (b) DSMC predictions for the pressure perturbation in response to $\omega=1$ adiabatic actuation (solid line, identical with the crosses in Fig. 4a), and vibro-thermal excitation with $U_0=1$ and $Q_0=\gamma/(2(\gamma-1))$ (dashed line). Results are presented at time $t=2\pi n/\omega$ $(n=1,2,\ldots)$.

$U_0=1$ and $Q_0=\gamma/(2(\gamma-1))$ are taken, to examine the system response to excitation at optimal sound-reduction conditions according to continuum-limit analysis (see Section 3.2).

Treating DSMC predictions as numerically "exact", the results in Fig. 4a indicate that neither the collisionless nor continuum limit analyses predict the system response correctly. To a limited extent, the collisionless results match with DSMC data for $x\lesssim 3$, where the effect of molecular collisions is relatively minor. The agreement with continuum-based results is not satisfactory (apart from for $x\gtrsim 13$, where the pressure signal has essentially vanished), as continuum description is not valid when the actuation frequency is of the order of the mean collision frequency. In view of the disagreement between DSMC and continuum-limit results, it is expected that the optimal conditions for sound reduction found for $\omega\ll 1$ will be far less effective at $\omega\sim O(1)$. This is indeed supported by the findings in Fig. 4b, which show only limited reduction in pressure amplitude when taking $Q_0=Q_0^{\mathrm{opt}}(\omega\ll 1)$ (cf. Fig. 3c).

The results in Fig. 4 are typical of the intermediate interval of frequencies, ranging between $0.5\lesssim\omega\lesssim 10$. With increasing frequency within this range, the system response varies between near-continuum and near-collisionless behavior. At the two extremes, the context meaning of the term "far field" varies, referring to infinitely large distances from the wall for $\omega\ll 1$, and small distances (of the order of mean free path and less) for $\omega\gg 1$.

4. Non-periodic excitation

The results in Section 3 have focused on the system response to single-frequency excitation. Having discussed the conditions for sound reduction at high and low frequencies in separate, we now consider the gas response to infinite-spectrum excitation. Specifically, we study the system reaction to impulse perturbation

$$U_w(t)=U_0\delta(t),\quad Q_w(t)=Q_0\delta(t) \tag{47}$$

where U_0 and Q_0 mark the amplitudes of mechanical and heat-flux inputs, respectively, and δ denotes Dirac's delta function. The choice of a delta-function excitation is appropriate for applying both collisionless and continuum schemes, as the signal duration is infinitely short. Collisionless predictions are expected to be valid at times shorter than the mean free time ($t\lesssim 1$), and continuum results should hold at long times ($t\gg 1$). In parallel with the periodic analysis presented in Section 3, the system response at short times is confined to the vicinity of the boundary and contains all frequency components of the delta function. With increasing time, the boundary-excited signal propagates away from the wall, and its form becomes more and more dominated by lower frequency contributions. DSMC predictions are not available for this case, as delta-function excitation cannot be easily simulated. Nevertheless, given the results presented in Section 3 and the above discussion, we consider the limit-case data to be quantitatively effective for $t\lesssim 1$ and $t\gg 1$. Detailed numerical solution is yet required to obtain the pulse propagation at intermediate $t\sim O(1)$ times.

4.1. Early-time response

Making use of the collisionless-flow analysis in Section 2.1, and substituting Eq. (47) into (13)–(16), the integrals appearing in (12) can be explicitly evaluated using familiar delta-function properties. Denoting

$$G_n=\int_0^\infty \delta(t-x/c_x)c_x^n\exp\left[-c_x^2\right]\mathrm{d}c_x=\frac{x^{n+1}}{t^{n+2}}\exp\left[-x^2/t^2\right], \tag{48}$$

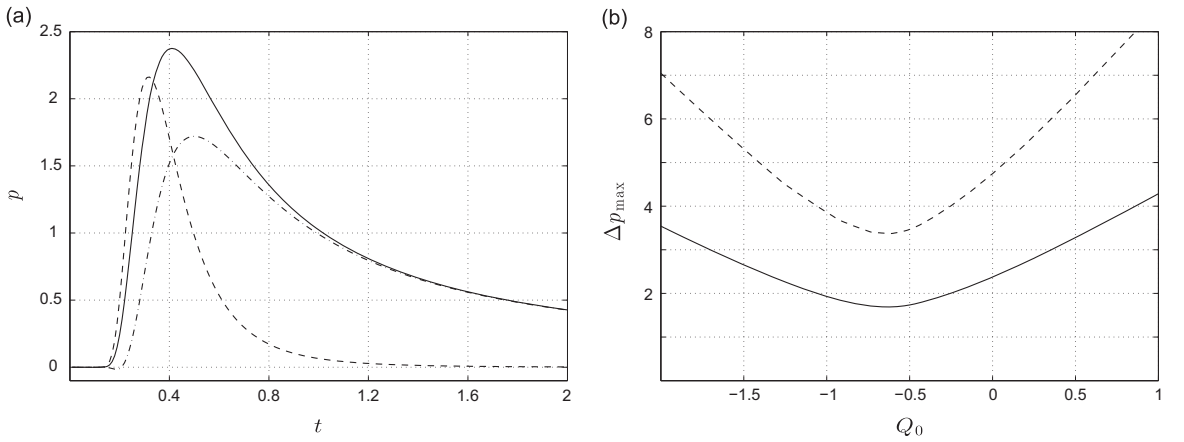

Fig. 5. Early-time response to delta-function excitation (see (47)): (a) time-variation of pressure fluctuation at $x=0.5$ in response to adiabatic ($U_0=1$ and $Q_0=0$, solid line), thermal ($U_0=0$ and $Q_0=1$, dashed line) and vibro-thermal ($U_0=1$ and $Q_0=-0.5$, dash-dotted line) excitations; (b) effect of heat-flux strength Q_0 on the maximal variation in acoustic pressure, $\Delta p_{\max}$, at fixed points (solid line for $x=0.5$, dashed line for $x=0.25$).

closed-form expressions for the hydrodynamic perturbations are obtained by substitution of (48) and (A.4) into (A.1)–(A.3). The result obtained is a causal description of the early-time system response to delta-function actuation, valid at times not exceeding the mean free time, $t\lesssim 1$.

Fig. 5 presents the early-time response, based on the collisionless solution, of the gas system to impulse excitation. Fig. 5a shows the time variation of pressure fluctuation at a fixed point, $x=0.5$, in response to adiabatic ($U_0=1$ and $Q_0=0$), thermal ($U_0=0$ and $Q_0=1$) and vibro-thermal ($U_0=1$ and $Q_0=-0.5$) excitations. Fig. 5b presents the effect of source heat strength, Q_0, on the change in pressure perturbation calculated at two fixed points ($x=0.5$ and $x=0.25$). Here, $\Delta p_{\max}$ marks the value of pressure difference between maximum and minimum values of p, obtained as the generated signal passes through the point. As an example, the value of $\Delta p_{\max}\approx 2.37$ given for $x=0.5$ and $Q_0=0$ in Fig. 5b corresponds to the difference between the maximum and minimum values of acoustic pressure in the solid line in Fig. 5a. This is used here as a measure for the acoustic perturbation generated by the boundary.

Comparing between the curves in Fig. 5a, we find that actuation- and heat-induced signals propagate qualitatively different at early times. While both responses contain a single peak in time (reflecting the maximum magnitude of pressure perturbation caused by the passage of exciting signal through the fixed point), later-time relaxation is much slower in the motion-induced case. This results in non-vanishing values of p at much longer times, where the collisionless description becomes invalid. Yet, focusing on times $t<1$, the different forms of solid and dashed curves indicate that no complete cancellation of the pressure signal may be achieved through simple superposition of the two responses. This is supported by the only partial pressure reduction obtained in the dash-dotted line in Fig. 5a, presenting the system response to $U_0=1$ and $Q_0=-0.5$ excitation. Recall that, in the counterpart periodic case discussed in Section 3.1, the results have shown that this choice leads to optimal pressure reduction.

The complete effect of heat-flux strength Q_0 on early-time acoustic pressure propagation, measured through the maximum value of pressure difference, $\Delta p_{\max}$, at a fixed point, is shown in Fig. 5b. At both points presented, $x=0.5$ and $x=0.25$, $\Delta p_{\max}$ is obtained minimal for $Q_0\approx -0.63$. This value differs from the optimal value found in the counterpart periodic case, $Q_0=-0.5$ (see Section 3.1). Pointing to the characteristic differences between the single-frequency and continuous-spectrum analyses, we recall that the high-frequency response in Section 3.1 describes a fast decaying wave, confined to the immediate vicinity of the boundary; in contrast, the delta function input contains the entire spectrum of frequencies, and the system response cannot be predicted based on the separate analyses of high- or low-frequency inputs discussed in Section 3. We further comment on this point at the end of Section 3.2.

4.2. Late-time response

To achieve the late-time behavior, the calculation follows the steps outlined in Section 2.2 with (47) as the input signal. In difference from the single frequency case, the time Fourier transform of the delta function

$$\overline{U}_w(\omega)=U_0,\quad \overline{Q}_w(\omega)=Q_0 \tag{49}$$

contains the entire spectrum of frequencies, distributed uniformly. Theoretically, the solution should collect single-frequency responses at all frequencies, $\omega\in(-\infty,\infty)$, and evaluate the time-domain solution through the inverse Fourier transform (32). Yet, for a numerical calculation, the infinite frequency domain needs to be truncated and discretized. We have therefore conducted the solution over the interval $\omega\in[-400,400]$, and verified that further increase in the range of frequencies, as well as refinement in the frequency grid, does not affect the results at the late times of interest.

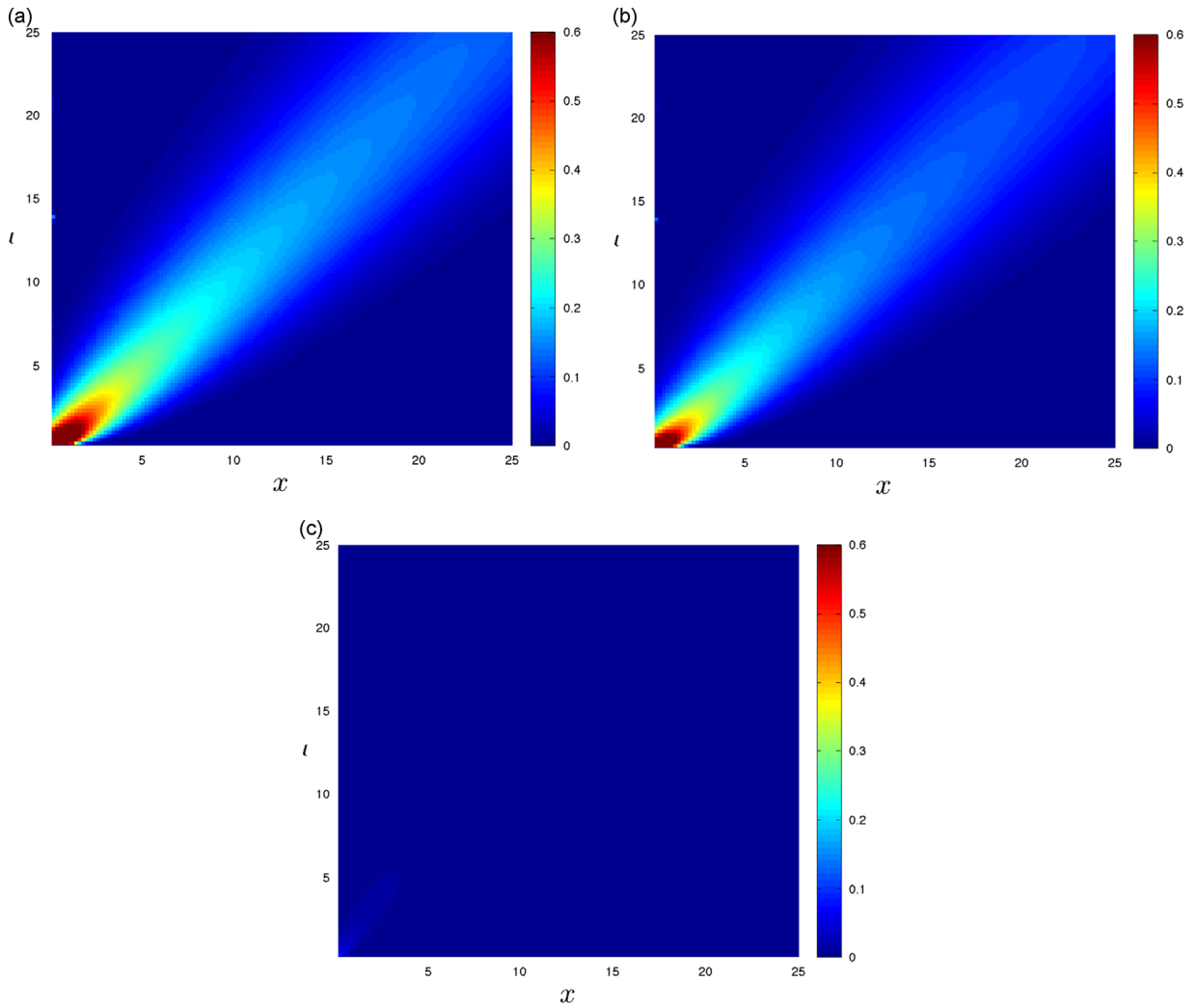

Fig. 6. Continuum-limit predictions for time–space maps of gas acoustic pressure in response to delta-function excitation (see (47)): (a) adiabatic-wall actuation ($U_0=1, Q_0=0$); (b) heat-flux excitation ($U_0=0, Q_0=1$); (c) optimal sound-reduction conditions ($U_0=1, Q_0=\gamma/(2(\gamma-1))$).

Fig. 6 presents time–space maps of gas acoustic pressure in response to impulse boundary excitation. The figure compares between cases of adiabatic-wall animation ($U_0=1$ and $Q_0=0$ in (47), Fig. 6a), heat-flux excitation ($U_0=0$ and $Q_0=1$, Fig. 6b), and optimal sound-reduction conditions ($U_0=1$ and $Q_0=\gamma/(2(\gamma-1))$, Fig. 6c). For clarity of presentation, the color scale in all figures is identical ($0\le p\le 0.6$), as well as the time and space intervals (both within $[0,25]$).

Starting with Fig. 6a and b, we observe a similar qualitative response to both types of excitation. The speed of signal propagation in both cases is obtained by tracking the location of maximum pressure fluctuation in time. Recalling the present scaling of time by l/U_{th}, the results confirm that the wave propagates in the speed of sound, so that the maximum acoustic pressure is located at $x\approx t\sqrt{2/\gamma}$ at time t. The waves in both scenarios decay with increasing time, reducing to about 10 percent of their initial strength at $t=25$. The only quantitative difference between the vibroacoustic and thermoacoustic responses is in the slightly lower amplitude of the latter. Following the discussion in Section 3.2, this magnitude difference is expected, since only a $(\gamma-1)/\gamma$ part of wall thermal energy is transformed into far-field sound in the case of heat-flux excitation.

The results in Fig. 6c present the system response to $U_0=1$ and $Q_0=\gamma/(2(\gamma-1))$ excitation, which were found optimal for sound reduction in the periodic case at continuum conditions. Having shown in Section 3.2 that these conditions do not depend on ω (as long as $\omega\ll 1$), our results confirm that the same conditions hold for a delta function input. The small pressure fluctuations observed in Fig. 6c correspond to an $O(\omega)$ correction of the low-frequency limit, mentioned at the end of Section 3.2. At late times, the contribution of high-frequency components (which is confined to the vicinity of the boundary; see Fig. 1) becomes vanishingly small, and the system response becomes dominated by its low-frequency contributions. This rationalizes the correlation between optimal conditions for sound reduction for periodic low-frequency and late-time delta-function excitations.

In closing, traversing back to the results in Section 4.1, and comparing between system impulse responses at $t \ll 1$ and $t \gg 1$, qualitative differences are found. Specifically, optimal sound reduction at early times is achieved at Q_0 values different from the counterpart high-frequency result. This is since, at short times after the impulse, the propagating signal contains the entire range of frequencies to a similar extent, inasmuch as the generating delta-function does. Efficient control of the acoustic pressure at these times requires reduction of the signal at all wave frequencies, including the intermediate domain of $\omega \sim O(1)$. This, however, can only be achieved to a limited extent using a single control parameter, and, additionally, causes the optimal value of Q_0 to be shifted from both high- and low-frequency values (see Fig. 5b).

5. Conclusion

We analyzed the effect of surface heating on sound radiation from a vibrating boundary. Focusing on a setup of an infinite planar wall interacting with a semi-infinite gas expanse, the system response to arbitrary (small-amplitude) vibro-thermal excitation was studied. For the case of a sinusoidally actuated surface, the superposed effect of boundary heat-flux excitation at a common frequency ω (in molecular collision frequency units) was examined. The entire range of frequencies was considered, revealing, depending on the ratio between excitation frequency and molecular collision frequency, different flow regimes. The two limit cases of $\omega \ll 1$ (continuum-flow conditions) and $\omega \gg 1$ (ballistic flow) were investigated analytically, based on continuum equations and collisionless Boltzmann equation, respectively. In between, an intermediate interval of frequencies $\omega \sim O(1)$ was analyzed numerically, based on the direct simulation Monte Carlo method. Seeking for optimal conditions for acoustic sound reduction, it was found that effective attenuation is obtained when boundary heat flux is applied at opposite phase to surface actuation. Amplitude-wise, conditions for minimization of the acoustic field vary: at low-frequencies, wave radiation extends over large distances from the wall, and optimal sound reduction is achieved when the ratio between wall-inserted thermal and kinetic energies $|E_q/E_k|_{\mathrm{opt}}$ equals $\gamma/(\gamma-1)$ (with γ denoting the ratio between gas specific heat capacities). At high frequencies, wall signal affects only a thin layer (of the order of the mean free path) in the vicinity of the boundary, and optimal attenuation is achieved when $|E_q/E_k|_{\mathrm{opt}} = 1$. The analysis was extended to study the system response to non-periodic excitation, for the specific case of a delta-function input. Making use of the collisionless- and continuum-limit analyses, early- and late-time system responses were calculated and rationalized. While conditions for optimal sound reduction at late times coincide with the low-frequency predictions in the periodic case, no counterpart agreement was found between early-time analysis and high-frequency periodic behavior.

Comparing between the limits of a high- and low-frequency excitation, the differences found in optimal conditions for system sound reduction are associated with order-of-magnitude variations in the acoustic wavelength. Given by $\lambda = 2\pi/\omega$ in mean-free-path units, the acoustic radiation extends over distances $x \gg 1$ from the source for $\omega \ll 1$, with a relatively slow decay rate of $\exp[-\omega^2 \kappa x]$, where κ is an $O(1)$ constant (see Eqs. (40)–(42) *et seq.*). Far-field radiation occurs at quasistatic conditions, where part of the wall heat-radiated energy is transferred into a change in gas internal energy and not into sound. This is in marked difference from the limit of high-frequency excitations, where wall signal penetrates only few wavelengths, and less than a mean free path, into the gas layer, with a decay rate of $(\omega x)^{1/3} \exp[-(\omega x)^{2/3}]$ (see Section 3.1). In the absence of the balancing mechanism of gas molecular collisions, wall thermal energy is fully transferred into sound, thus making the mechanism of sound reduction via heating more efficient in this case. Our numerical analysis quantitates the system behavior in between the two limits (for $\omega \sim O(1)$ excitation), where smooth transition between continuum and ballistic responses is observed. Notably, the system reaction to impulse excitation, studied in Section 4, reflects the above limit-case analyses to only a limited extent: while the late-time system behavior (where input wavefront has propagated a distance $x \gg 1$ from the wall) matches with the low-frequency periodic predictions, early time response combines effects from the entire spectrum of frequencies, and thus cannot be attributed to any of the limits in separate. In view of traditional classifications of acoustic-field investigations into "near-field" and "far-field" descriptions, we find that both collisionless and continuum-limit analyses are valid in the entire (near and far) gas domain, as long as the flow conditions are in agreement with the model setup assumptions. Thus, in difference from common acoustic-field investigations, where only the far-field system behavior is discussed, the present solution is found advantageous in that it supplies the entire response of the gas. In this respect, the collisionless and continuum analyses can be considered complementary to achieve the full description of the system at a wide range of flow conditions.

While direct comparison of our findings with experimental observation is currently unavailable, the present work aims at supplying rationalization and reference comparison with existing knowledge. To this end, the far-field approximation of the continuum solution in Eqs. (38) and (43) matches well with an expected wave-like behavior of the solution, propagating away from the boundary with the speed of sound. In addition, the low-frequency optimal conditions (43) for sound reduction in the periodic case are found in agreement with a quasistatic energy balance based on first-law considerations. At the other extreme of collisionless flow regime, established results regularly appear in a confined (double-wall) domain (e.g., Ref. [17]), where the length-scale is inevitably small. Yet, a thin-layer response of a confined system to high-frequency excitations (by direct variation in the boundary temperature) has been previously reported (see Refs. [22,23]). All of the above, together with the close agreement of our results with numerical predictions by the DSMC method, lend support of the validity of the present findings.

In terms of classical acoustics, the differences found between optimal conditions for system sound reduction at different flow regimes can be expressed through variations in the required monopole source strengths of boundary actuation and heating, U_0 and Q_0 (see Eqs. (38) and (43)). In addition to the common discussion of active noise control methodologies in

continuum mechanics [4,5,24], the present investigation considers the effect of deviation from continuum conditions on the results, and supplies quantitative description for the entire (near and far field) sound propagation mechanism in all rarefaction regimes. Considering the relative complexity of analyzing non-continuum flows, this is made possible due to the simplified planar setup considered. Study of the problem at two-dimensional and non-planar (curved) geometries, which are desired extensions of the present work, are topics for future investigation.

Appendix A. High-frequency approximation for collisionless-flow response

Substituting (34) together with (11) and (33) into (12), and then into (13)–(16), we obtain the following high-frequency approximations for the hydrodynamic perturbations:

$$\rho(x,t)\approx\frac{1}{\sqrt{\pi}}\left[2U_0G_1+R_0G_0+\Theta_0\left(G_2-\frac{1}{2}G_0\right)\right], \tag{A.1}$$

$$u(x,t)\approx\frac{1}{\sqrt{\pi}}\left[2U_0G_2+R_0G_1+\Theta_0\left(G_3-\frac{1}{2}G_1\right)\right], \tag{A.2}$$

$$p(x,t)\approx\frac{2}{3\sqrt{\pi}}\left[2U_0(G_3+G_1)+R_0(G_2+G_0)+\Theta_0\left(G_4+\frac{1}{2}(G_2+G_0)\right)\right] \tag{A.3}$$

and $T(x,t)\approx p-\rho$. In (A.1)–(A.3),

$$R_0=\sqrt{\pi}\left(\frac{7}{8}U_0-Q_0\right)\quad\text{and}\quad\Theta_0=\sqrt{\pi}\left(\frac{1}{4}U_0+2Q_0\right). \tag{A.4}$$

References

[1] G. Rossing, N.H. Fletcher, *Principles of Vibration and Sound*, Springer, New York, 2004.
[2] A. Schwarz, J.E. Janicka, *Combustion Noise*, Springer, New York, 2009.
[3] D.J. Mead, *Passive Vibration Control*, Wiley, Chichester, 2000.
[4] P.A. Nelson, S.J. Elliott, *Active Control of Sound*, Academic Press, MA, USA, 1991.
[5] C. Hansen, S. Snyder, *Active Control of Noise and Vibration*, CRC Press, Boca Raton, Florida, 1997.
[6] H. Shinoda, T. Nakajima, K. Ueno, N. Koshida, Thermally induced ultrasonic emission from porous silicon, *Nature* 400 (1999) 853–855.
[7] F. Kontomichos, A. Koutsioubas, J. Mourjopoulos, N. Spiliopoulos, A. Vradis, A thermoacoustic device for sound reproduction, *Journal of the Acoustical Society of America* 123 (2008) 3707.
[8] H. Hu, T. Zhu, J. Xu, Model for thermoacoustic emission from solids, *Applied Physics letters* 96 (2010) 214101.
[9] C.W. Lim, L.H. Tong, Y.C. Li, Theory of suspended carbon nanotube thinfilm as a thermal-acoustic source, *Journal of Sound and Vibration* 332 (2013) 5451–5461.
[10] D. Zhao, M. Rayhanoglu, Feedback control of acoustic disturbance transient growth in triggering thermoacoustic instability, *Journal of Sound and Vibration* 333 (2014) 3639–3656.
[11] C. Ji, D. Zhao, S. Li, X. Li, Numerical simulation of passive control of self-excited thermoacoustic instabilities by using a secondary heater, *Proceedings of the 21st International Congress on Sound and Vibration*, 2014.
[12] L. Sirovich, J.K. Thurber, Propagation of forced sound waves in rarefied gasdynamics, *Journal of the Acoustical Society of America* 37 (1965) 329–339.
[13] S.K. Loyalka, T.C. Cheng, Sound-wave propagation in a rarefied gas, *Physics of Fluids* 22 (1979) 830–836.
[14] S. Stefanov, P. Gospodinov, C. Cercignani, Monte carlo simulation and Navier–Stokes finite difference calculation of unsteady-state rarefied gas flows, *Physics of Fluids* 10 (1998) 289–300.
[15] N.G. Hadjiconstantinou, Sound wave propagation in transition-regime micro- and nanochannels, *Physics of Fluids* 14 (2002) 802–809.
[16] A. Manela, G.A. Radtke, L. Pogorelyuk, On the damping effect of gas rarefaction on propagation of acoustic waves in a microchannel, *Physics of Fluids* 26 (2014) 032001.
[17] A. Manela, L. Pogorelyuk, Cloaking via heating: *approach to acoustic cloaking of an actuated boundary in a rarefied gas*, *Physics of Fluids* 26 (2014) 062003.
[18] M.N. Kogan, *Rarefied Gas Dynamics*, Plenum, New-York, 1969.
[19] Y. Sone, *Molecular Gas Dynamics: Theory, Techniques, and Applications*, Birkhäuser, Boston, 2007.
[20] G. Bird, *Molecular Gas Dynamics and the Direct Simulation of Gas Flows*, Clarendon, Oxford, 1994.
[21] M. Abramowitz, Evaluation of the integral $\int_0^\infty e^{-u^2-x/u}du$, *Journal of Mathematical Physics* 32 (1953) 188–192.
[22] A. Manela, N.G. Hadjiconstantinou, Gas motion induced by unsteady boundary heating in a small-scale slab, *Physics of Fluids* 20 (2008) 117104.
[23] A. Manela, N.G. Hadjiconstantinou, Gas-flow animation by unsteady heating in a microchannel, *Physics of Fluids* 22 (2010) 062001.
[24] M.S. Howe, *Acoustics of Fluid-Structure Interactions*, Cambridge University Press, Cambridge, 1998.